Journal of Environmental Management 308 (2022) 114635

Contents lists available at ScienceDirect

Journal of Environmental Management

journal homepage: www.elsevier.com/locate/jenvman

Insight into the role of temperature, time and pH in the effective zirconium retention using clay minerals

Esperanza Pavón [a,b], María D. Alba [a,*]

[a] Instituto Ciencia de los Materiales de Sevilla (CSIC-US), Avda. Americo Vespucio, 49, 41092, Sevilla, Spain
[b] Departamento de Física de la Materia Condensada, Universidad de Sevilla, Avda. Reina Mercedes s/n, 41012, Sevilla, Spain

ARTICLE INFO

Keywords:
Clay minerals
Zirconium
Uranium
Radioactive waste disposal

ABSTRACT

The use of zirconium in chemical industries generates a potential risk of Zr contamination in the environment, with particular concern for the decommissioning of uranium-graphite reactors. Among the natural adsorbents employed for the treatment of nuclear waste, clay minerals showed a very high affinity adsorption for radionuclides, but the influence of the chemical composition, pressure, temperature and time reaction have not yet been analysed on deep. Thus, the objective of this research is to explore several experimental conditions for an actual prediction of the behaviour of zirconium immobilization by clay minerals. The results have shown that factors such as zirconium cation nature (Zr^{4+} or ZrO^{2+}), temperature, time and pH influence the extent of zirconium immobilization by clay minerals and the zirconium phases generated. At moderate conditions, zirconium tectosilicates are formed and evolve to zircon at high temperature and a longer time reaction.

1. Introduction

Increasing demands for nonconventional energy sources, the worldwide Paris Agreement and the need to reduce the reliance on fossil fuels have driven attention to nuclear energy again, due to its efficient and cost-effective power production. However, the management of radioactive waste generated during the fission process is the biggest concern when using this energy source.

In nuclear power plants, graphite reactors cladding is constructed with zirconium alloys, which allows a low neutron-capture cross section and resistance to corrosion under normal service conditions (Brown et al., 2005). However, its use implies the emission of ^{93}Zr ($t_{1/2} = 1.5 \times 106$ years) after the irradiation and consequently this isotope should be considered in nuclear waste management (Shoesmith and Zagidulin, 2011).

Several natural adsorbents have been employed for the treatment of nuclear waste. Among them, clay minerals stand out due to their high affinity adsorption for radionuclides and low water permeability (Kotlyarevskiy et al., 2016; Yapar et al., 2015). In fact, they have been selected as the engineering barrier in the expected deep geological repositories (DGR) for the disposal of high-level radioactive waste (HLRW) disposal (Cuevas et al., 2018). Moreover, their availability, low cost, and high stability under oxidizing and reducing conditions and high cation exchange capacity (CEC) have made them excellent adsorbent materials for all kind of pollutants (Stathi et al., 2007).

Recently, Montes et al. (2021) observed that zirconium cation type, ZrO^{2+} or Zr^{4+}, influenced the main zirconium retention mechanisms under subcrital conditions. Their results showed that precipitation/crystallization was the main retention mechanism when ZrO^{+2} was involved whereas new zirconium silicate phases were formed after the interaction of Zr^{4+} with clay minerals.

However, the hydrothermal conditions conducted in those experiments (300 °C, 7 days, and 8.59 MPa) were not the ones expected in the DGR currently under consideration. For example, the initial expected storage temperature in the DGR is expected to be lower than 200 °C, with temperatures falling below 150 °C several hundred years after the emplacement (Ojovan and Lee, 2014; Poinssot et al., 1996). In addition to temperature, other important parameters, such as pH, time, or metallic ions present in the solution, should be explored in terms of security (Abdel Hakam Mahdy and Ghazala, 2019; Guo et al., 2020; Şenol et al., 2021). Thus, for an actual prediction of the behavior of zirconium inmobilization by clay minerals, it is necessary to explore the influence of parameters such as temperature, pH and time.

* Corresponding author.
E-mail address: alba@icmse.csic.es (M.D. Alba).

https://doi.org/10.1016/j.jenvman.2022.114635
Received 9 November 2021; Received in revised form 26 January 2022; Accepted 27 January 2022
Available online 1 February 2022

2. Experimental section

2.1. Materials

The clay mineral samples examined were 2:1 phyllosilicates: two different bentonites (FEBEX and MX80) considered suitable buffer material in HLRW repositories (Rao and Ravi, 2013) and one saponite. This latter was chosen because previous researchers demonstrated that trioctahedral smectites with aluminium in tetrahedral sheet enhanced their HLRW retention properties (Alba et al., 2001a, 2001b).

FEBEX bentonite was extracted from the Cortijo de Archidona deposit (Almera, Spain). Processing in the factory consisted of disaggregation and gentle grinding, drying at 60 °C and sieving by 5 mm (ENRESA, 2006, 2000). The montmorillonite content in FEBEX bentonite was 90–92% (Fernandez et al., 2004). Based on chemical analyses, the structural formula of the FEBEX smectite is: $(Ca_{0.5}Na_{0.08}K_{0.11})$ $(Si_{7.78}Al_{0.22})$ $(Al_{2.78}Fe^{III}_{0.33}Fe^{II}_{0.02}Mg_{0.81})O_{20}(OH)_4$ (Fernandez et al., 2004).

MX80 bentonite was extracted from Wyoming (USA) and supplied in the form of powder (Madsen, 1998). The batch used in this investigation was mainly composed of montmorillonite (83%) (Villar et al., 2012). Based on chemical analyses, the structural formula is: $(Na_{0.36}Ca_{0.20})$ $(Si_{7.96}Al_{0.04})$ $(Al_{3.1}Mg_{0.56}Fe^{III}_{0.18}Fe^{II}_{0.16})O_{20}(OH)_4$ (Montes-H et al., 2005).

Saponite has been obtained from the Source Clay Minerals Repository University of Missouri (Columbia) and has the following chemical formula: $Na_{0.61}K_{0.02}Ca_{0.09}$ $(Si_{7.2}Al_{0.8})^{IV}(Mg_{5.79}Fe_{0.15})$-$^{VI}O_{20}(OH)_4$ (Alba et al., 2001a).

$ZrO(NO_3)_2{\cdot}7H_2O$ (CAS 14985-18-3) and $Zr(SO_4)_2{\cdot}4.5H_2O$ (CAS 34806-73-0), which are commercially available from Sigma-Aldrich, have been used in this work as possible chemical analogues of uranyl and tetravalent actinides presents in HLRW (Chapman and Smellie, 1986).

2.2. Hydrothermal reaction

Three hundred milligrams of clay minerals were added to 3.65 mmol of zirconium salts (mmol zirconium: mmol smectite 11.2 ± 0.6), suspended in 50 ml of water and heated, in a stainless steel reactor, at 300 °C or 150 °C between 2 days and 16 weeks; the experimental details are summarized in Table 1. All experiments were carried out at natural pH, pH = 1.4 for $ZrO^{2+}$and 1.0 for Zr^{4+}. After hydrothermal treatment at 300 °C, the pH was 0.5 for $ZrO^{2+}$and 5.0 for Zr^{4+} and after hydrothermal treatment at 150 °C, the pH was 2.0. Furthermore, the experiment with $ZrO(NO_3)_2$ at 300 °C for 2 days was repeated by previously adjusting the pH with a 0.5 M NH4OH solution at a value of 4.5. The reaction products were collected by filtering, washed with distilled water, and dried at room temperature (RT). The samples were named Zr-*x*-y-*T*-*t*-z; where *x* is the zirconium source, N for $ZrO(NO_3)_2$ or S for $Zr(SO_4)_2$; *y* is the clay minerals, SAP, FEB or MX; *T* is the temperature; *t* is the time; and; *z* indicates if the pH has been adjusted, null (without pH correction) or pH (with pH correction).

Table 1
Samples name and experimental variables.

Samples[a]	Zr source	pH	T (° C)	T	Variable[b]
Zr–N-*X*-300-2d-pH	$ZrO(NO_3)_2$	4.5	300	2d	pH
Zr–N-*X*-300-2d	$ZrO(NO_3)_2$	1.4	300	2d	pH, t
Zr–N-*X*-300-7d	$ZrO(NO_3)_2$	1.4	300	7d	t
Zr–S-*X*-300-2d	$Zr(SO_4)_4$	1.4	300	2d	t, T
Zr–S-*X*-300-7d	$Zr(SO_4)_4$	1.4	300	7d	t
Zr–S-*X*-150-16w	$Zr(SO_4)_4$	1.4	150	16w	T

[a] *X* = FEB (FEBEX), MX (MX80) or SAP (Saponite).
[b] pH = pH variable, t = time variable, and, T = temperature variable.

2.3. Characterization techniques

X-ray diffraction (XRD) patterns were obtained in the X-ray laboratory (CITIUS, University of Seville, Spain) on a Bruker D8 Advance instrument equipped with a Cu Kα radiation source operating at 40 kV and 40 mA. Diffractograms were obtained in the 2θ range of 3–70° with a step size of 0.015° and a step time of 0.1 s.

Single-pulse (SP) MAS NMR spectra were recorded in the Nuclear Magnetic Resonance Unit at the University of Cordoba (Spain) on a Bruker AVANCE WB400 spectrometer equipped with a multinuclear probe. Powdered samples were packed in 3.2 mm zirconia rotors and spun at 10 kHz. ^{29}Si MAS NMR spectra were acquired at a frequency of 79.49 MHz, using a pulse width of 2.7 μs (π/2 pulse length = 7.1 μs) and delay times of 3 s ^{27}Al MAS-NMR spectra were recorded at 104.26 MHz with a pulse width of 0.92 μs (π/2 pulse length = 9.25 μs) and a delay time of 0.1 s. Chemical shift values were reported in ppm from tetramethylsilane for ^{29}Si and from a 0.1 M $AlCl_3$ solution for ^{27}Al. Spectra were simulated using the DMFIT software (Massiot et al., 2002), Gaussian-Lorentzian model was used for all the peaks, and linewidth, position, and amplitude were the fitted parameters.

3. Results

3.1. XRD analysis

The XRD pattern of untreated FEBEX (Fig. 1a) exhibits typical montmorillonite reflections with a series of narrow and sharp peaks indicating its crystalline structure. The basal spacing, d_{001}, is 1.49 nm due to bilayer hydrated Ca^{2+} in the interlayer space (El Mrabet et al., 2014). Additionally, quartz reflections are observed.

Treatment with $ZrO(NO_3)_2$ and $Zr(SO_4)_2$ at natural pH (Fig. 1b, c, and 1e, 1f, 1g) causes total disruption of the smectite framework and the disappearance of the quartz impurity. Additionally, new phases are observed, mainly baddeleyite, monoclinic ZrO_2, accompanied by zircon, ZrSiO4, and kaolinite as minor phases. In Zr–S-FEB-300-2d and Zr–S-FEB-300-7d (Fig. 1e and f), a remnant montmorillonite with a basal spacing, d_{001}, of 1.52 nm is observed, due to the replacement of the

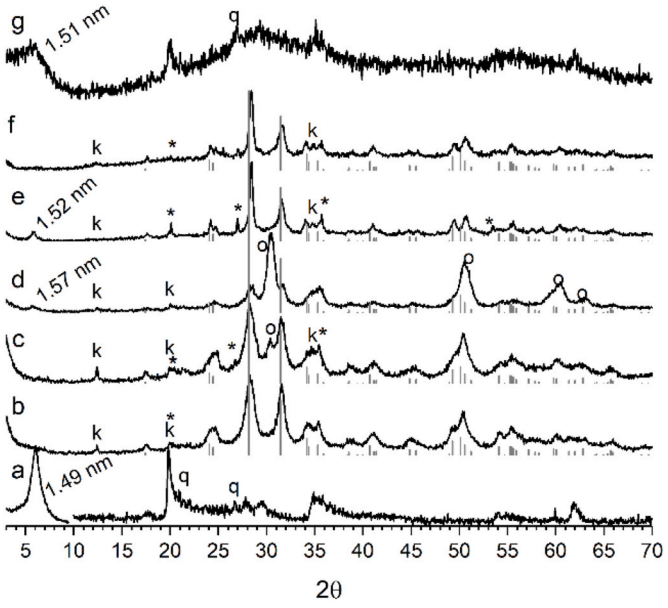

Fig. 1. XRD of a) raw FEBEX bentonite, b) Zr–N-FEB-300-2d, c) Zr–N-FEB-300-7d, d) Zr–N-FEB-300-2d-pH, e) Zr–S-FEB-300-2d, f) Zr–S-FEB-300-7d, and g) Zr–S-FEB-150-16w. Lines = baddeleyite (monoclinic ZrO_2) PDF 00-037-1484; * = zircon ($ZrSiO_4$) PDF 04-007-5058; o = cubic ZrO_2 PDF 04-015-0098; k = kaolinite PDF 00-001-0527; and q = quartz PDF 00-003-0419.

initial interlayer cations with leached octahedral Al^{3+}or/and Zr^{4+}. The same basal spacing, d_{001} = 1.57 nm, is observed when the initial pH of the $ZrO(NO_3)_2$ solution is adjusted to 4.5 (Fig. 1d, Zr–N-FEB-300-2d-pH). In this sample, the main crystalline ZrO_2 phase is the cubic polymorph instead of the monoclinic one. Additionally, all of the XRD patterns show a background due to the presence of noncrystalline phases. This background is more evident in the sample treated at 150 °C for 16 weeks (Zr–S-FEB-150-16w), where nearly no crystalline phases can be observed, only small reflections due to montmorillonite and quartz (Fig. 1g).

Similar results are found for MX80 samples (Fig. 2). The XRD pattern of untreated MX80 (Fig. 2a) exhibits typical reflections of montmorillonite with a series of narrow and sharp peaks indicating its crystalline structure. The basal spacing is ca. 1.21 nm is mainly due to one-layer hydrate monovalent cations in the interlayer space (Bergaya et al., 2006; Grim, 1968). In addition, reflections of quartz and tridymite are observed. Treatment with $ZrO(NO_3)_2$ and $Zr(SO_4)_2$ at natural pH (Fig. 2b, c and 2e, 2f, 2g) provokes the same lamellar disturbance as in the FEBEX samples and the consequent disappearance of the smectite framework. On the contrary, the quartz and trydimite impurities do not completely disappear in Zr–N-MX-300-2d and Zr–N-MX-300-7d (Fig. 2b and c). Baddeleyite, accompanied by minor phases (kaolinite and zircon, $ZrSiO_4$) are also present.

The lame structure is poorly conserved when the initial pH of $ZrO(NO_3)_2$ solution is adjusted to 4.5 (Fig. 2d, Zr–N-MX-300-2d-pH) and the remnant montmorillonite shows a basal spacing of 1.53 nm. In this sample, the main crystalline ZrO_2 phase is the cubic polymorph, accompanied by kaolinite, zircon, and baddeleyite as minor phases. The residual montmorillonite is also observed in the samples treated with $Zr(SO_4)_2$ at 300 °C for 2 days (Fig. 2e, Zr–S-MX-300-2d), Its basal spacing is 1.46 nm, probably due to the replacement of the initial interlayer cations with leached octahedral Al^{+3} and/or Zr^{+4}. Additionally, all the XRD patterns show a background due to the presence of noncrystalline phases, as well as in the FEBEX samples, which is more evident in the sample treated at 150 °C for 16 weeks, Zr–S-MX-150-16w, where nearly no crystalline phases can be observed, only small reflections due to montmorillonite and quartz.

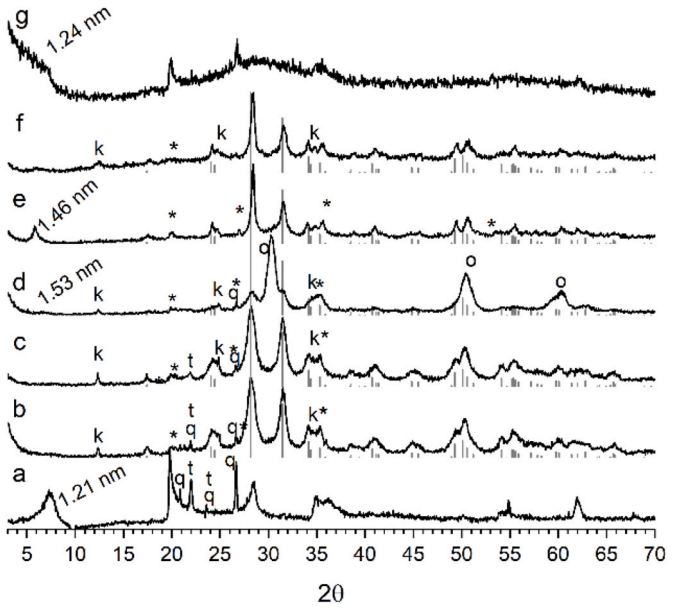

Fig. 2. XRD of a) raw MX80 bentonite, b) Zr–N-MX-300-2d, c) Zr–N-MX-300-7d, d) Zr–N-MX-300-2d-pH, e) Zr–S-MX-300-2d, f) Zr–S-MX-300-7d, and g) Zr–S-MX-150-16w. Lines = baddeleyite (monoclinic ZrO_2) PDF 00-037-1484; * = zircon ($ZrSiO_4$) PDF 04-007-5058; o = cubic ZrO_2 PDF 04-015-0098; k = kaolinite PDF 00-001-0527; q = quartz PDF 00-003-0419 and t = trydimite PDF 04-011-3620.

Pristine saponite shows an XRD pattern (Fig. 3a) characterized by two distinct types of reflection, general and basal ones. The basal spacing of 1.21 nm corresponds to the one-layer hydrate Na^+ cations in the interlayer space (Bergaya et al., 2006; Grim, 1968). As observed in the bentonites FEBEX and MX80, treatment at natural pH and 300 °C with $ZrO(NO_3)_2$ and $Zr(SO_4)_2$ causes total disruption of the structure of the smectite (Fig. 3b, c and 3e, 3f) with the presence of residual saponite in the Zr–S-SAP-300-2d sample (Fig. 3e). In this case, the basal spacing is ca. 1.46 nm, is higher than the base spacing of the pristine sample, probably due to the replacement of the initial interlayer cations with a leached framework cation and/or Zr^{4+}. In all of these treatments, secondary phases emerge after treatment, mainly baddelyite and zircon. When pH is adjusted, Zr–N-SAP-300-2d-pH, remnant saponite is also observed in the XRD pattern (Fig. 3d) with a base spacing of 1.47 nm. In the last case, cubic ZrO_2 is also observed. All XRD patterns show a background due to the presence of noncrystalline phases that is more evident in the sample treated at lower temperature (150 °C) and higher time (16 weeks), Fig. 3g. In this last sample, some small reflections due to remnant saponite with basal spacing of 1.41 nm is also observed.

3.2. NMR spectra analysis

^{29}Si MAS NMR spectrum of the untreated FEBEX bentonite (Fig. 4a, left) shows two sets of signals. The main one is in the range of −100 to −80 ppm and is due to typical Q^3 (mAl) environment of smectite, and, ii) the second one is in the range of −100 to −115 ppm and is due to Q^4 (mAl) of the impurities (Engelhardt and Michel, 1987). The deconvolution parameters of the ^{29}Si MAS NMR spectrum (Table S1) show that the contribution of the smectite contribution to the ^{29}Si MAS NMR spectrum (Fig. 4a) reaches 90%. The Q^3 (mAl) signals of smectite are centred at −93.85 ppm, Q^3(0Al), and −87.32 ppm, Q^3(1Al), which is compatible with a dioctahedral configuration and with an isomorphical substitution of Si by Al in the tetrahedral sheet (Alba et al., 2001b).

^{27}Al MAS NMR spectrum of the untreated FEBEX bentonite (Fig. 4a, right) shows a main resonance centred at approximately 0 ppm, due to the octahedral Al environment and compatible with the dioctahedral character of the montmorillonite (Engelhardt and Michel, 1987). Additionally, a small signal between 50 and 70 ppm is observed, due to

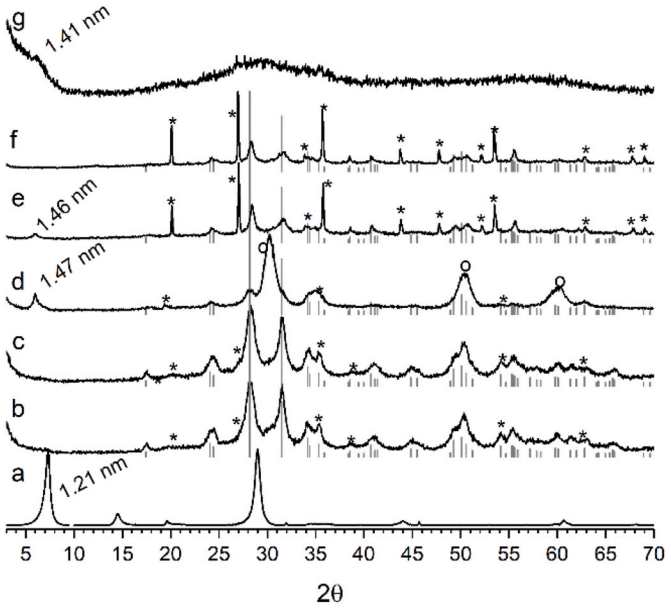

Fig. 3. XRD of a) raw saponite, b) Zr–N-SAP-300-2d, c) Zr–N-SAP-300-7d, d) Zr–N-SAP-300-2d-pH, e) Zr–S-SAP-300-2d, f) Zr–S-SAP-300-7d, and g) Zr–S-SAP-150-16w. Lines = baddeleyite (monoclinic ZrO_2) PDF 00-037-1484; * = zircon ($ZrSiO_4$) PDF 04-007-5058; o = cubic ZrO_2 PDF 04-015-0098.

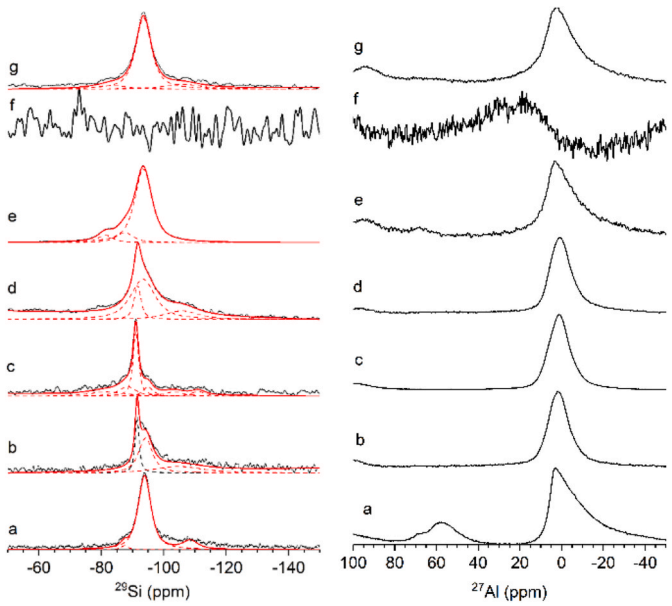

Fig. 4. ^{29}Si (left) and ^{27}Al (right) MAS NMR spectra of a) raw FEBEX bentonite, b) Zr–N-FEB-300-2d, c) Zr–N-FEB-300-7d, d) Zr–N-FEB-300-2d-pH, e) Zr–S-FEB-300-2d, f) Zr–S-FEB-300-7d, and, g) Zr–S-FEB-150-16w.

Al in tetrahedral coordination (Engelhardt and Michel, 1987). This last signal is made up of two signals; the main one at ca. 57 ppm due to q^4 environment of the impurities observed in the XRD diagrams, and the very small one at ca. 65 ppm due to q^3 environment in smectite phase (Engelhardt and Michel, 1987).

After treatment, a complete transformation of the ^{29}Si MAS NMR spectra is observed (Fig. 4b–g, left).

^{29}Si MAS NMR spectrum of Zr–N-FEB-300-7d is deconvoluted into six peaks (Fig. 4c, left, and Table S1). Signals corresponding to zirconium silicates are observed: i) one at ca. −81 ppm of $ZrSiO_4$, 4.4%; and; ii) two peaks at ca. −103 ppm and ca. −88 ppm due to Q^4(1Zr) and Q^4(2Zr), respectively, (Ferreira et al., 2001; Lin and Rocha, 2004; Mackenzie and Smith, 2002). The total contribution of Zr environments is c. a. 14%.

In this spectrum, Q^3(0Al) signal of montmorillonite shifts to −95 ppm; this shift together with the absence of Q^3(1Al) indicate the leaching of the tetrahedral aluminium (Alba et al., 2001b). A new Q^3 environment is observed at about. −91 ppm, which corresponds to the transformation of montmorillonite, 2:1 phyllosilicate, to kaolinite, 1:1 phyllosilicate (Mantovani et al., 2009) and accounts with a 66.8%. Finally, signals at ca. −111 ppm is observed and corresponds to tridymite (Mackenzie and Smith, 2002).

The deconvolution of ^{29}Si MAS NMR spectra of Zr–N-FEB-300-2d and Zr–N-FEB-300-2d-pH (Fig. 4b and d, left and Table S1) shows that the main environment corresponds to Q^3(0Al) signal of montmorillonite, 48.3% and 67.5%, respectively. Also signals of kaolinite and Q^4(1Zr) are observed. Signal corresponding to Q^4(1Zr) decreases when pH is corrected.

^{27}Al MAS NMR spectra of bentonite FEBEX after hydrothermal treatment with $ZrO(NO_3)_2$ (Fig. 4b–d, right) show a unique aluminium symmetric resonance at ca. 0 ppm, due to six-coordinated aluminium. The position at ca. 0 ppm and the low quadrupolar line shape of the band (symmetry band) are compatible with aluminum in the octahedral sheet of kaolinite (Engelhardt and Michel, 1987). The absence of both tetrahedral resonances is compatible with the disruption of the smectite framework (or its dissolution) and with the dissolution of the q^4 impurities of the initial samples.

The ^{29}Si MAS NMR spectrum of Zr–S-FEB-300-2d (Fig. 4e, left) is characterized by a main signal at ca. −94 ppm with small signals mainly at higher chemical shifts. The spectrum is the convolution of three signals: i) signals at ca. −93.5 and −87.6 ppm due to Q^3(0Al) and Q^3(1Al) of the remnant montmorillonite, and, ii) a signal at −81.3 due to $ZrSiO_4$ (Cota et al., 2013). Its ^{27}Al MAS NMR spectrum (Fig. 4e, right) shows a main asymmetric resonance centred at ca. 0 ppm, due to the octahedral Al environment and a small signal at ca. 70 ppm due to the tetrahedral aluminium of the remnant montmorillonite (Engelhardt and Michel, 1987).

Severe damage in short range order is observed after hydrothermal treatment of FEBEX with $Zr(SO_4)_2$ at 300 °C for 7 days and no ^{29}Si MAS NMR signal is observed in its spectrum (Fig. 4f, left). The ^{27}Al MAS NMR spectrum (Fig. 4f, right) has a very low S/N ratio and shows a very broad band at ca. 0 ppm due to aluminium in octahedral coordination (Engelhardt and Michel, 1987).

The ^{29}Si MAS NMR spectrum of Zr–S-FEB-150-16w (Fig. 4g, left) is characterized by a main signal at ca. −94 ppm with small signals mainly at lower chemical shifts. This spectrum is the convolution of three signals: i) signal at ca. −93.5 ppm due to remnant montmorillonite, and, ii) two signals at −83.4 and −106.4 ppm due to Q^4 (nZr) (Ferreira et al., 2001; Lin and Rocha, 2004; Mackenzie and Smith, 2002). Its ^{27}Al MAS NMR spectrum (Fig. 4g, right) shows a main asymmetric resonance centred at ca. 0 ppm, due to the octahedral Al environment of the remnant montmorillonite (Engelhardt and Michel, 1987).

^{29}Si MAS NMR spectrum of the pristine MX80 (Fig. 5a, left) is quite similar to that of FEBEX but the deconvolution parameters (Table S2) show that the Si smectite environments are different in both bentonites. The ^{29}Si MAS NMR spectrum of MX80 shows a symmetric signal at −93.66 ppm due to Q^3(0Al), reaching 77.8% of the total Si of the spectrum. The absence of Q^3(1Al) environment is due to the lack of substitution of Si by Al in the tetrahedral sheet. The ^{29}Si MAS NMR spectrum is compatible with its mineralogical composition (Montes-H et al., 2005).

The ^{27}Al MAS NMR spectrum of MX80 (Fig. 5a, right) shows a main resonance centred at ca. 0 ppm, due to the octahedral Al environment and compatible with the dioctahedral character of montmorillonite (Engelhardt and Michel, 1987). Additionally, there is a small signal at ca. 57 ppm, due to q^4 environment of impurities, is also observed (Engelhardt and Michel, 1987).

The ^{29}Si MAS NMR spectra after the hydrothermal treatment with

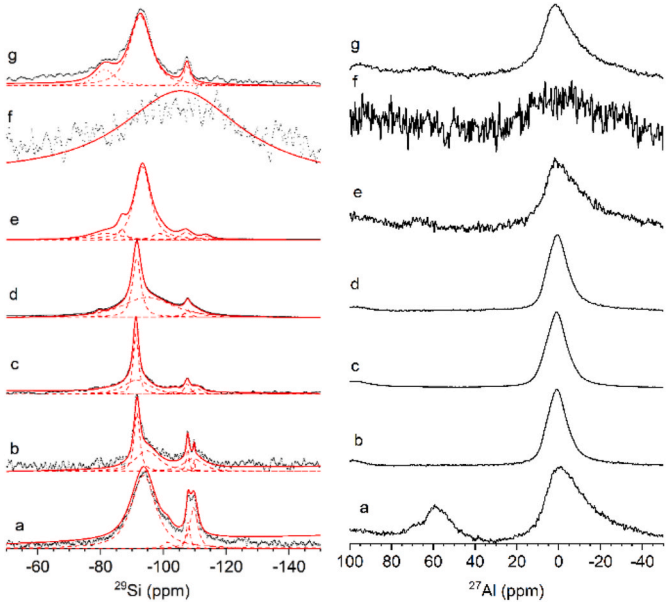

Fig. 5. ^{29}Si (left) and ^{27}Al (right) MAS NMR spectra of a) raw MX80 bentonite, b) Zr–N-MX-300-2d, c) Zr–N-MX-300-7d, d) Zr–N-MX-300-2d-pH, e) Zr–S-MX-300-2d, f) Zr–S-MX-300-7d, and, g) Zr–S-MX-150-16w.

$ZrO(NO_3)_2$ (Fig. 5b–d, left) are characterized by a main narrow signal at high frequency accompanied by other minor signals at lower frequency.

The spectrum of Zr–N-MX-300-7d is deconvoluted into six peaks (Fig. 5c, left, and Table S2). Several signals corresponding to zirconium silicates are observed: i) one at ca. −81 ppm of $ZrSiO_4$ (Cota et al., 2013), 3.5%; and; ii) two peaks at ca. −104 ppm and ca. −92 ppm due to Q^4(1Zr) and Q^4(2Zr), respectively (Ferreira et al., 2001; Lin and Rocha, 2004; Mackenzie and Smith, 2002), and the total Q^4 (nZr) is 44.6%.

The montmorillonite signal is absent but a new Q^3 environment is observed at ca. −91 ppm, which corresponds to the transformation of montmorillonite, 2:1 phyllosilicate, to kaolinite, 1:1 phillosilicate (Mantovani et al., 2009) and accounts with a 38.4%. Finally, signals at ca. −111 ppm and at ca. −108 ppm are observed as due to tridymite and quartz (Mackenzie and Smith, 2002), respectively.

The deconvolution of ^{29}Si MAS NMR spectra of Zr–N-MX-300-2d and Zr–N-MX-300-2d-pH (Fig. 5b and d, left and Table S2) shows that the main environment corresponds to Q^3(0Al) signal of montmorillonite, a 41.5% and 61.7%, respectively. Among montmorillonite, signals of kaolinite, trydimite, and quartz are also observed. The signal corresponding to $ZrSiO_4$ is only observed when the pH has been corrected.

The ^{27}Al MAS NMR spectra of bentonite MX80 after hydrothermal treatment with $ZrO(NO_3)_2$ (Fig. 5b–d, right) show a unique aluminium symmetric resonance at ca. 0 ppm, due to six-coordinated aluminium. The position at ca. 0 ppm and the low quadrupolar line shape of the band (symmetry band) are compatible with aluminum in the octahedral sheet of kaolinite (Engelhardt and Michel, 1987). The absence of both tetrahedral resonances is compatible with the disruption of the smectite framework (or its dissolution) and with the dissolution of the q^4 impurities of the initial samples.

The ^{29}Si MAS NMR spectrum of Zr–S-MX-300-2d (Fig. 5e, left) is characterized by a main signal at ca. −94 ppm with small signals on both sides. The spectrum is the convolution of six signals: i) a signal at ca. −92.7 ppm due to remnant montmorillonite, ii) a new Q^3 environment is observed at ca. −93 ppm due to kaolinite, iii) signals at ca. −113 ppm and at ca. −107 ppm due to tridymite and quartz, and finally, iv) two signals at −81.8 ppm and −86.8 ppm due to zircon and Q^4(2Zr) respectively. Its ^{27}Al MAS NMR spectrum (Fig. 5e, down-right) is very noisy and shows a main asymmetric resonance centred at ca. 0 ppm, due to the octahedral Al environment of the remnant montmorillonite and a small signal of the tetrahedral aluminium (Engelhardt and Michel, 1987).

Severe damage in short range order is observed after hydrothermal treatment of MX80 with $Zr(SO_4)_2$ at 300 °C for 7 days, but it is less severe than in FEBEX (Fig. 5f). Only a very broad symmetric signal is observed at ca. −104 ppm in the ^{29}Si MAS NMR spectrum, that could be interpreted that the main Si environment corresponded to Q^4 (1Zr) environment (Ferreira et al., 2001; Lin and Rocha, 2004; Mackenzie and Smith, 2002) but it has not been able to be quantified. The ^{27}Al MAS NMR spectrum has a very low S/N ratio and shows a very broad band at ca. 0 ppm due to aluminium in octahedral coordination (Engelhardt and Michel, 1987).

The ^{29}Si MAS NMR spectrum of Zr–S-MX-150-16w (Fig. 5g, left) is characterized by a main signal at ca. −94 ppm with small signals on both sides. The band is the convolution of three signals (Table S2): i) a signal at ca. −92.7 ppm due to remnant montmorillonite, and, ii) two signals at −81.3 ppm and −107.5 ppm due to zircon and quartz respectively (Ferreira et al., 2001; Lin and Rocha, 2004; Mackenzie and Smith, 2002). Its ^{27}Al MAS NMR spectrum (Fig. 5g, right) shows a main asymmetric resonance centred at ca. 0 ppm, due to the octahedral Al environment of the remnant montmorillonite and the small signal of the tetrahedral aluminium (Engelhardt and Michel, 1987).

The ^{29}Si MAS NMR spectrum of the pristine saponite (Fig. 6a, left) is characterized by three main signals at −95.8, −90.8 and −85.0 ppm corresponding to Q^3 (mAl), $0 \leq m \leq 2$, in an intensity ratio of 10:4.6:0.22 (Alba et al., 2001b) (Table S3). From these results, the Si/Al ratio can be calculated (Engelhardt et al., 1981) as 8.9, which is in good agreement with the chemical composition, Si/Al = 9.0. The ^{27}Al MAS NMR spectrum of the untreated saponite (Fig. 6a, right) shows a unique signal centred at 65 ppm due to tetrahedral aluminium, q^3(3Si) (Engelhardt and Michel, 1987).

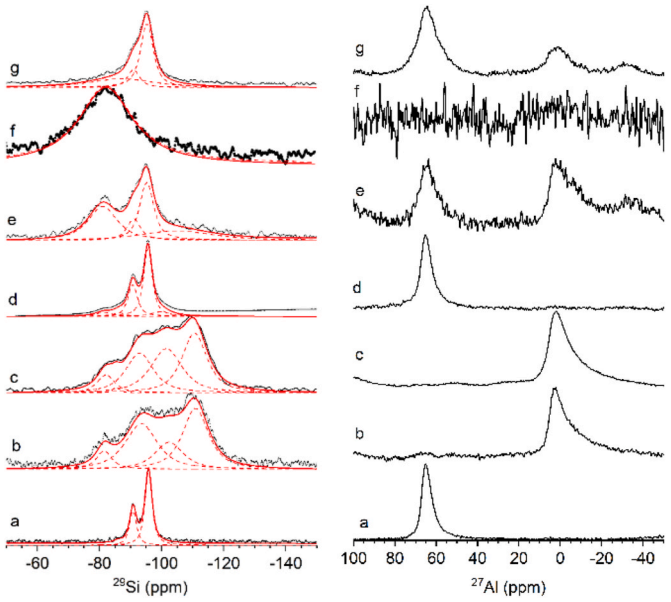

Fig. 6. ^{29}Si (left) and ^{27}Al (right) MAS NMR spectra of a) raw saponite, b) Zr–N-SAP-300-2d, c) Zr–N-SAP-300-7d, d) Zr–N-SAP-300-2d-pH, e) Zr–S-SAP-300-2d, f) Zr–S-SAP-300-7d and, g) Zr–S-SAP-150-16w.

The ^{29}Si MAS NMR spectra of saponite treated with $ZrO(NO_3)_3$ at natural pH (Fig. 6b–c, left) are characterized by a broad band in the range between −120 ppm and −70 ppm. This broad band is the convolution of several peaks (Table S3). The peak was at ca. −82 ppm corresponds to zircon (Cota et al., 2013) and accounts with the 10.7% and 7.0% for treatment during 7 and 2 days, respectively. And the peaks at lower chemical shifts correspond to Si Q^4 (nZr), n = 0, 1 and 2 (Ferreira et al., 2001; Lin and Rocha, 2004; Mackenzie and Smith, 2002), which are not crystalline because those zeolite species are not observed by XRD. The ^{27}Al MAS NMR spectra (Fig. 6b–c, right) are characterized by a narrow signal at ca. 0 ppm due to aluminium in octahedral coordination (Engelhardt and Michel, 1987) and corroborates the total disruption of the saponite framework as previously observed by XRD.

When pH is corrected, Zr–N-SAP-300-2d-pH, the ^{29}Si and ^{27}Al MAS NMR spectra (Fig. 6d) are quite similar to those of the pristine saponite, in agreement with the XRD that evidenced the remnant saponite, but a small contribution of 6.1% of Si due to zircon is observed (Table S3).

The ^{29}Si MAS NMR spectrum of Zr–S-SAP-300-2d (Fig. 6e, left) is characterized by a main signal at ca. −94 ppm with small signals on both sides. This band is the convolution of four signals (Table S3): i) two signals at ca. −95.2 ppm and −91.1 ppm due to remnant saponite accounting for 41.1% of the total Si, ii) a signal at ca. −81.8 ppm due to zircon, and, iii) a signal at −104.6 ppm due to Q^4(1Zr). Its ^{27}Al MAS NMR spectrum (Fig. 6e, right) is very noise-free and shows a remnant signal of tetrahedral aluminium and an asymmetric resonance centred at ca. 0 ppm, due to the octahedral Al environment of the leached framework aluminium (Engelhardt and Michel, 1987).

The ^{29}Si MAS NMR spectrum of Zr–S-SAP-300-7d (Fig. 6f, left) is characterized by a broad symmetric band at ca. −81 ppm that corresponds to zircon (Cota et al., 2013) and accounts with the 100% of the total Si environment (Table S3). No signal in the ^{27}Al MAS NMR spectrum (Fig. 6f, right) is observed due to the total disruption of the saponite framework and the leaching of aluminium to the supernatant.

Finally, the ^{29}Si MAS NMR spectrum of Zr–S-SAP-150-16w (Fig. 6g,

left) is quite similar to that of raw saponite, but with a boarder linewidth due to partial disruption of the saponite framework as corroborated by ^{27}Al MAS NMR spectroscopy. ^{27}Al MAS NMR spectrum (Fig. 6g, right) exhibits a main Al environment due to tetrahedral aluminium as saponite but more asymmetric than the original one and, additionally, a small signal at ca. 0 ppm is observed due to six-coordinated leached aluminium. The deconvolution of the ^{29}Si spectrum (Table S3) shows a contribution of 33.6% of the Q^4(2Zr) among Si environment of saponite.

4. Discussion

4.1. pH effect

Independent of pH value, the interaction of zirconyl with clays at 300 °C for 2 days under hydrothermal conditions caused the disruption of the layered structure of the smectites and the formation of new phases.

At the lowest pH, the amount of remnant smectite for both bentonites (Zr–N-FEB-300-2d and Zr–N-MX-300-2d) was lower than at pH 4.5 (Zr–N-FEB-300-2d-pH and Zr–N-MX-300-2d-pH), Table S1-S2 (Alba et al., 2010), and this smectite was no crystalline (Figs. 1c and 2c). When pH was corrected to 4.5, the smectite framework remained with hydrated ZrO^{2+} as interlayer cation (Figs. 1d and 2d). Part of the smectite structure (2:1 phyllosilicate) was transformed into kaolinite (1:1 phyllosilicate), with this transformation highest at natural pH (Table S1-S2), as previously observed in bentonites that reacted with chemical analogous of actinides (Osuna et al., 2015).

In the case of saponite, non-remnant smectite was observed at the lowest pH, Zr–N-SAP-300-2d, (Table S3); as a consequence the aluminium framework was leached (Fig. 6c, right) and tectosilicate, Q^4(4Si), was generated (Table S3). When the pH was corrected to 4.5 (Zr–N-SAP-300-2d,-pH), the amount of remnant smectite was ca. 98% (Table S3) and the basal space was compatible with hydrated ZrO^{2+} as interlayer cation (Fig. 3d). As a difference from bentonite, non-transformation of 2:1 phyllosilicate to 1:1 phyllosilicate was observed due to the trioctahedral character of the saponite. As previously reported, bentonites evolve to saponitic clay minerals under the corrosion environment expected in the DGR (Cuevas et al., 2018), indicating a higher stability of these clay minerals.

The main crystalline phase was ZrO_2 as previously reported for the heating of zirconium salt solutions (Kim and Kim, 1995) but different polymorphs were observed at different pH values. Monoclinic ZrO_2 was mainly crystallized at pH 1.4 and cubic ZrO_2 at pH 4.5. Jada and Peletis (Jada and Peletis, 1989) reported that the pH of the precursor solution had a marked influence on polymorphic phase formation or transformation and crystallite growth in gel-derived ZrO_2 powders. The prevalence of the monoclinic polymorph is in good agreement with the stability range of ZrO_2 observed in the thermal decomposition of zirconium salts to generate ZrO_2 (Stefanic et al., 1996). A small amount of crystalline zircon was also observed in saponite at both pH values and accounted for 6–7% of total Si.

Furthermore, other non-crystalline zirconium silicates such as tectosilicates (Q^4(1Zr)), in FEBEX bentonite and saponite or $ZrSiO_4$, were observed in MX80 at pH 4.5. The amount of tectosilicates was higher at the lowest pH value. Thus, the waste forms depend on the solution chemistry and local acidity/alkalinity, as observed by Guo et al. (2020).

In general, the amount of immobilized zirconium increased at the lowest pH value and was accompanied by a higher disruption of the smectite structure, saponite being the most reactive clay minerals as previously reported by Alba et al. (Alba et al., 2001a, 2001b).

4.2. Effect of the reaction time

The interaction of ZrO^{2+} or Zr^{4+} with clays at 300 °C under hydrothermal conditions caused the disruption of the layered structure of the smectite, which was transformed into kaolinite in the case of bentonites (Figs. 1–3). The smectite Q^3 environments decreased, with increasing of the kaolinite Q^3 environment as reaction time increased, being this transformation higher when the final pH was lower (Table S1-S3). Only in the case of treatment at 300 °C, 2 days with Zr^{4+} (Figs. 1e, 2e and 3e) a small portion of crystalline smectite (approx. 40% of Si of saponite, Table S3) was observed and it contained hydrated Zr^{4+} in the interlayer space.

For bentonites, the main crystalline phase was monoclinic ZrO_2 and a small amount of crystalline zircon, $ZrSiO_4$, being favoured in the reaction with Zr^{4+} (Table S1-S2). In saponite, the main crystalline phase depended on the nature of the zircon cation and was monoclinic ZrO_2 for reaction with ZrO^{2+} and $ZrSiO_4$ for reaction with Zr^{4+}.

The formation of zirconium-containing tectosilicates was favoured in the treatment with ZrO^{2+} for FEBEX and with Zr^{4+} for MX80 (Table S1-S2). At a long reaction time, the decrease in tectosilicate was accompanied by the formation of $ZrSiO_4$. In addition, The formation of zirconium-containing tectosilicates containing zirconium was observed in saponite (Table S3). No influence was observed on the total amount of zirconium silicate phases with time or cation nature; however, the longer time and Zr^{4+} favoured the formation of $ZrSiO_4$ vs zirconium tectosilicates, as previously reported in the literature (Montes et al., 2021).

4.3. Effect of temperature

At both temperatures, the layered structure of the smectites broke down (Figs. 1–3f and 1-3g), the smectite Q^3 environment decreased with increasing temperature (Table S1-S3) and the interlayer hydrated Zr^{4+} balanced the layer charge. At 150 °C, the non-crystalline phase was observed being 300 °C for the crystallization of monoclinic ZrO_2 and a minor amount of crystalline zircon, $ZrSiO_4$ and monoclinic ZrO_2, in saponite.

At low temperature, zirconium tectosilicates were formed and completely transformed into zircon at high temperature and were the predominant phase in MX80 (Table S1-S3).

5. Conclusions

The experimental factors such as cation nature, temperature, time and pH value influence the extent of immobilization of zirconium by clay minerals and the zirconium phases generated.

The reaction time or nature of the zirconium cation do not influence the total amount of zirconium silicate phases. However, immobilized zirconium increased at the lowest pH, making saponite the most reactive clay minerals.

At low temperature, zirconium tectosilicates were formed and completely transformed into zircon at high temperature. A similar effect was observed at long reaction time. In general, Zr^{4+} favoured the formation of $ZrSiO_4$ and ZrO^{2+} the formation of zirconium tectosilicates.

Finally, immobilization of zirconium was possible both by bentonites and by saponite even under extreme conditions.

Credit author statement

Esperanza Pavón: Formal analysis, Writing – review & editing. María D Alba: Project administration, Formal analysis, Writing – original draft, Writing – review & editing.

Declaration of competing interest

The authors declare that they have no known competing financial interests or personal relationships that could have appeared to influence the work reported in this paper.

Acknowledgments

We thank ENRESA for their economical support. Dr. Pavón thanks the University of Seville for the financial support of her current contract from the VI PPIT-US program.

Appendix A. Supplementary data

Supplementary data to this article can be found online at https://doi.org/10.1016/j.jenvman.2022.114635.

References

Abdel Hakam Mahdy, R., Ghazala, R., 2019. Evaluation study for uranium adsorption from gattar pilot plant pregnant solution by Egyptian bentonite sediments. Arab J. Nucl. Sci. Appl. 52, 211–220. https://doi.org/10.21608/ajnsa.2018.4302.1101.

Alba, M.D., Becerro, A.I., Castro, M.A., Perdigon, A.C., 2001a. Hydrothermal reactivity of Lu-saturated smectites: Part I. A long-range order study. Am. Mineral. 86, 115–123.

Alba, M.D., Becerro, A.I., Castro, M.A., Perdigón, A.C., 2001b. Hydrothermal reactivity of Lu-saturated smectites: Part II. A short-range order study. Am. Mineral. 86, 124–131.

Alba, M.D., Castro, M.A., Chain, P., Orta, M.M., Pazos, M.C., Pavón, E., 2010. Hydrothermal stability of layered silicates in neutral and acidic media: effect on engineered-barrier safety. Clay Clay Miner. 58, 501–514.

Bergaya, F., Theng, B.K.G., Lagaly, G., 2006. Handbook of Clay Science. Elsevier.

Brown, P.L., Curti, E., Grambow, B., Ekberg, C., 2005. Chemical Thermodynamics of Zirconium. oecd Nuclear Energy Agency.

Chapman, N.A., Smellie, J.A.T., 1986. Conditions around a final repository for high-level radioactive-waste - introduction and summary of the workshop. Chem. Geol. 55, 167–173.

Cota, A., Burton, B.P., Chaín, P., Pavón, E., Alba, M.D., 2013. Solution properties of the system ZrSiO4-HfSiO4: a computational and experimental study. J. Phys. Chem. C 117, 10013–10019.

Cuevas, J., Ruiz, A.I., Fernández, R., González-Santamaría, D., Angulo, M., Ortega, A., Torres, E., Turrero, M.J., 2018. Authigenic clay minerals from interface reactions of concrete-clay engineered barriers: a new perspective on MG-clays formation in alkaline environments. Minerals 8. https://doi.org/10.3390/min8090362.

El Mrabet, S., Castro, M.A., Hurtado, S., Orta, M.M., Pazos, M.C., Villa-Alfageme, M., Alba, M.D., 2014. Effect of clays and metal containers in retaining Sm3+ and ZrO2+ and the process of reversibility. Am. Mineral. 99, 696–703. https://doi.org/10.2138/am.2014.4665.

Engelhardt, G., Lohse, U., Lippmaa, E., Tarmak, M., Magi, M., 1981. Si-29 NMR investigations of silicon-aluminum ordering in the aluminosilicate framework of faujasite-type zeolites. Zeitschrift fur Anorg. und Allg. Chemie 478, 239–240.

Engelhardt, G., Michel, D., 1987. High Resolution Solid State NMR of Silicates and Zeolites. John Wiley and Sons, New York.

ENRESA, 2006. Full-scale Engineered Barriers Experiment (Madrid).

ENRESA, 2000. Full-scale Engineered Barriers Experiment for a Deep Geological Repository for High Level Radioactive Waste in Crystalline Host Rock (Madrid).

Fernandez, A.M., Baeyens, B., Bradbury, M., Rivas, P., 2004. Analysis of the porewater chemical composition of a Spanish compacted bentonite used in an engineered barrier. Phys. Chem. Earth 29, 105–118.

Ferreira, P., Ferreira, A., Rocha, J., Soares, M.R., 2001. Synthesis and structural characterization of zirconium silicates. Chem. Mater. 13, 355–363.

Grim, R.E., 1968. Clay Mineralogy (New York).

Guo, X., Gin, S., Lei, P., Yao, T., Liu, H., Schreiber, D.K., Ngo, D., Viswanathan, G., Li, T., Kim, S.H., Vienna, J.D., Ryan, J.V., Du, J., Lian, J., Frankel, G.S., 2020. Self-accelerated corrosion of nuclear waste forms at material interfaces. Nat. Mater. 19 https://doi.org/10.1038/s41563-019-0579-x.

Kim, D.J., Kim, H., 1995. Effect of Zirconium salts on the hydrous ZrO2 coating of SIC whiskers. Mater. Lett. 23, 113–116.

Kotlyarevskiy, S.G., Pavliuk, A.O., Zakharova, E.V., Volkova, A.G., 2016. Capability assessment for application of clay mixture as barrier material for irradiated zirconium alloy structure elements long-term processing for storage during decommissioning of uranium-graphite nuclear reactors. IOP Conf. Ser. Mater. Sci. Eng. 135 https://doi.org/10.1088/1757-899X/135/1/012020.

Lin, Z., Rocha, J., 2004. Small-pore framework zirconium and hafnium silicates with the structure of mineral tumchaite. Microporous Mesoporous Mater. 76, 99–104.

Mackenzie, H.J.D., Smith, M.E., 2002. Multinuclear Solid-State NMR of Inorganic Materials. Pergamon Materials Series, Amsterdam.

Madsen, F.T., 1998. Clay mineralogical investigations related to nuclear waste disposal. Clay Miner. 33, 109–129.

Mantovani, M., Escudero, A., Alba, M.D., Becerro, A.I., 2009. Stability of phyllosilicates in Ca(OH)2 solution: influence of layer nature, octahedral occupation, presence of tetrahedral Al and degree of crystallinity. Appl. Geochem. 24, 1251–1260.

Massiot, D., Fayon, F., Capron, M., King, I., Le Calve, S., Alonso, B., Durand, J.O., Bujoli, B., Gan, Z.H., Hoatson, G., 2002. Modelling one- and two-dimensional solid-state NMR spectra. Magn. Reson. Chem. 40, 70–76. https://doi.org/10.1002/mrc.984.

Montes-H, G., Fritz, B., Clement, A., Michau, N., 2005. Modelling of geochemical reactions and experimental cation exchange in MX80 bentonite. J. Environ. Manag. 77, 35–46.

Montes, L., Pavón, E., Cota, A., Alba, 2021. Zirconium retention for minimizing environmental risk: role of counterion and clay mineral. Chemosphere 267, 128914. https://doi.org/10.1016/j.chemosphere.2020.128914.

Ojovan, M.I., Lee, W.E., 2014. Performance Assessment, an Introduction to Nuclear Waste Immobilisation (Amsterdam).

Osuna, F.J., Chain, P., Cota, A., Pavón, E., Alba, M.D., 2015. Impact of hydrothermal treatment of FEBEX and MX80 bentonites in water, HNO3 and Lu(NO3)3 media: implications for radioactive waste control. Appl. Clay Sci. 118, 48–55.

Poinssot, C., Goffe, B., Magonthier, M.C., Toulhoat, P., 1996. Hydrothermal alteration of a simulated nuclear waste glass: effects of a thermal gradient and of a chemical barrier. Eur. J. Mineral 8, 533–548.

Rao, S.M., Ravi, K., 2013. Hydro-mechanical characterization of Barmer 1 bentonite from Rajasthan, India. Nucl. Eng. Des. 265, 330–340. https://doi.org/10.1016/j.nucengdes.2013.09.012.

Şenol, Z.M., Şimşek, S., Özer, A., Şenol Arslan, D., 2021. Synthesis and characterization of chitosan–vermiculite composite beads for removal of uranyl ions: isotherm, kinetics and thermodynamics studies. J. Radioanal. Nucl. Chem. 327, 159–173. https://doi.org/10.1007/s10967-020-07481-2.

Shoesmith, D.W., Zagidulin, D., 2011. The corrosion of zirconium under deep geologic repository conditions. J. Nucl. Mater. 418, 292–306. https://doi.org/10.1016/j.jnucmat.2011.07.028.

Stathi, P., Litina, K., Gournis, D., Giannopoulos, T.S., Deligiannakis, Y., 2007. Physicochemical study of novel organoclays as heavy metal ion adsorbents for environmental remediation. J. Colloid Interface Sci. 316, 298–309.

Stefanic, G., Music, S., Popovic, S., Furic, K., 1996. Formation of ZrO2 by the thermal decomposition of zirconium salts. Croat. Chem. Acta 69, 223–239.

Villar, M.V., Gomez-Espina, R., Gutierrez-Nebot, L., 2012. Basal spacings of smectite in compacted bentonite. Appl. Clay Sci. 65 (66), 95–105. https://doi.org/10.1016/j.clay.2012.05.010.

Yapar, S., Ozdemir, G., Fernandez Solarte, A.M., Torres Sanchez, R.M., 2015. Surface and interface properties of lauroyl sarcosinate-adsorbed CP+-montmorillonite. Clay Clay Miner. 63, 110–118.